

Cold Fronts by Merging of Shocks

Yuval Birnboim¹, Uri Keshet^{1*} & Lars Hernquist¹

¹*Harvard-Smithsonian Center for Astrophysics, 60 Garden Street, Cambridge, MA 02138 USA*

Accepted —. Received —; in original —

ABSTRACT

Cold fronts (CFs) are found in most galaxy clusters, as well as in some galaxies and groups of galaxies. We propose that some CFs are relics of merging between two shocks propagating in the same direction. Such shock mergers typically result in a quasi-spherical, factor $\approx 1.4 - 2.7$ discontinuity in density and in temperature. These CFs may be found as far out as the virial shock, unlike what is expected in other CF formation models.

As a demonstration of this effect, we use one dimensional simulations of clusters and show that shock induced cold fronts form when perturbations such as explosions or mergers occur near the cluster’s centre. Perturbations at a cluster’s core induce periodic merging between the virial shock and outgoing secondary shocks. These collisions yield a distinctive, concentric, geometric sequence of CFs which trace the expansion of the virial shock.

Key words: galaxies: clusters: general – galaxies: haloes – X-rays: galaxies: clusters – shock waves

1 INTRODUCTION

Recent X-ray observations of galaxy clusters reveal various phenomena in the gaseous haloes of clusters, such as mergers, cavities, shocks and cold fronts (CFs). CFs are thought to be contact discontinuities, where the density and temperature jump, while the pressure remains continuous (up to projection/resolution effects). They are common in clusters (Markevitch & Vikhlinin 2007) and vary in morphology (they are often arcs but some linear or filamentary CFs exist), contrast (the density jump is scattered around a value of ~ 2), quiescence (some are in highly disturbed merging regions, and some in smooth, quiet locations), and orientation (some are arcs around the cluster centres, and some are radial, or spiral in nature). CFs have been postulated to originate from cold material stripped during mergers (Markevitch et al. 2000, for example) or sloshing of the intergalactic medium (IGM; Markevitch et al. 2001; Ascasibar & Markevitch 2006). In some cases, a metallicity gradient is observed across the CF, indicating that it results from stripped gas, or radial motions of gas (see Markevitch & Vikhlinin 2007, and references therein). Shear is often found along CFs in relaxed cluster cores, implying nearly sonic bulk flow beneath (towards the cluster’s core) the CF (Keshet et al. 2009). Whether CFs are present at very large radii ($\gtrsim 500$ kpc) is currently unknown because of observational limitations.

Cold fronts are not rare. Markevitch et al. (2003) find

CFs in more than half of their cool core clusters, suggesting that most, if not all such clusters harbor CFs (Markevitch & Vikhlinin 2007). Ghizzardi et al. (2010) survey a sample of 42 clusters using XMM-Newton and find that 19 out of 32 nearby ($z < 0.075$) clusters host at least one CF. Based on observational limitations, and orientations of cold fronts, they conclude that this is a lower limit. While many CFs are directly attributed to mergers, out of 23 clusters in their sample that seem relaxed, 10 exhibit cold fronts. These 10 have systematically lower central entropy values. Another useful compilation of clusters for which cold fronts have been observed can be found in Owers et al. (2009). Out of the 9 high-quality Chandra observations of clusters with observed cold fronts, 3 of them, RXJ1720.1+2638, MS1455.0+2232 and Abel 2142 have non-disturbed morphologies.

In what follows, we propose that some CFs are produced by merging of shocks. When two shocks propagating in the same direction merge, a CF is always expected to form. Its parameters can be calculated by solving the shock conditions and corresponding Riemann problem. Most of the scenarios in which shocks are produced (quasars, AGN jets, mergers) predict that shocks will be created at, or near, a cluster centre, and expand outwards (albeit not necessarily isotropically). When a secondary shock trails a primary shock, it always propagates faster (supersonically with respect to the subsonic downstream flow of the primary shock), so collisions between outgoing shocks in a cluster are inevitable if they are generated within a sufficiently short time interval. We note that contact discontinuities can also form from head

* Einstein fellow

on collisions between shocks, and various other geometrical configurations. We restrict ourselves in this paper to merging of two shock propagating in roughly the same direction.

In § 2 we solve for the parameters of CFs that are caused by merging two arbitrary planar shocks. We show results of shock-tube hydrodynamic simulation that agree with the calculated analytical prediction. In § 3, we describe our spherical hydrodynamic simulations and realistic cluster profiles that are later used to investigate how these shocks may be produced, and discuss various ways to produce shocks in cluster settings. We identify two general mechanisms that create shocks in clusters: energetic explosions near the centre, or changes and recoils in the potential well of the cluster that correspond to various merger events. These mechanisms are simulated in § 4.1 and § 4.2 and also serve to demonstrate the robustness of the shock induced cold fronts (SICFs) that form. In § 5 we follow cluster growth and accretion over a Hubble time by using self-consistent 1D hydrodynamic simulations of gas and dark-matter. The virial shock that naturally forms serves as a primary shock, and we demonstrate that SICFs form when secondary shocks propagating from the centre merge with it. We show that oscillations of this shock around its steady state position can produce a series of SICFs. In § 6 we discuss aspects regarding the stability and sustainability of cold fronts in general, and derive some observational predictions that could serve to distinguish between CFs produced via this and other mechanisms. In § 7 we discuss our findings and conclude. Compact expressions for SICF parameters can be found in appendix § A.

2 MERGING OF TWO TRAILING SHOCKS

In this section we examine two planar shocks propagating in the same direction through a homogeneous medium and calculate the parameters of the contact discontinuity that forms when the second shock (secondary) overtakes the leading (primary) one. This problem is fully characterized (up to normalization) by the Mach numbers of the primary and secondary shocks, M_0 and M_1 . At the instant of collision, a discontinuity in velocity, density and pressure develops, corresponding to a Riemann problem (second case in Landau & Lifshitz 1959, §93). The discontinuity evolves into a (stronger) shock propagating in the initial direction and a reflected rarefaction wave, separated by a contact discontinuity which we shall refer to as a shock induced CF (SICF). The density is higher (and the entropy lower) on the SICF side closer to the origin of the shocks. In spherical gravitational systems, this yields a Rayleigh-Taylor stable configuration if the shocks are expanding outwards. Now, we derive the discontinuity parameters.

2.1 The Discontinuity Contrast

We consider an ideal gas with an adiabatic index γ . Before the shocks collide, denote the unshocked region as zone 0, the region between the two shocks as zone 1, and the doubly shocked region as zone 2 (these definitions are demonstrated schematically in fig. 1). After the merging, regions 0 and 2 remain intact, but zone 1 vanishes and is replaced by two regions, zone 3_o (the outer region for outgoing spherical

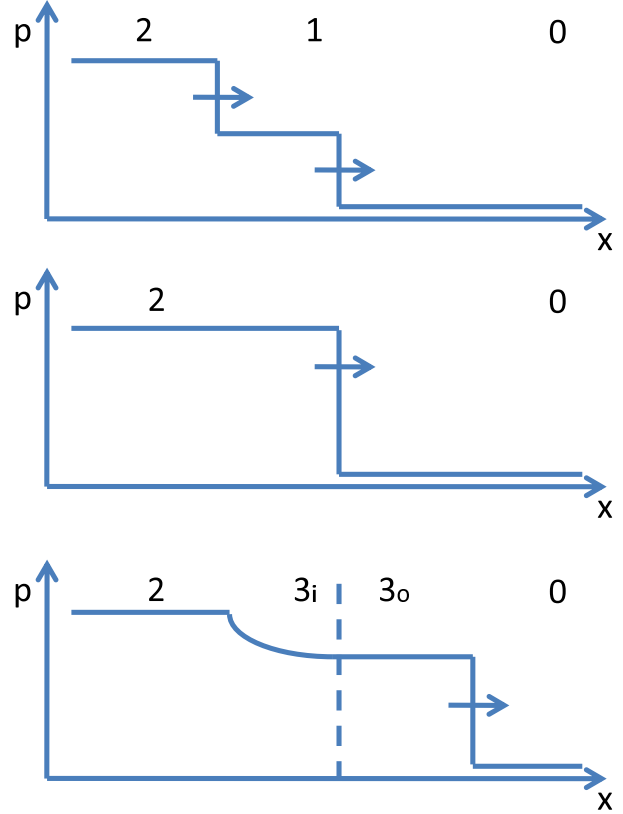


Figure 1. Schematics of shock merging. Pressure p is shown vs. an arbitrary spatial coordinate x , which is not fixed between the panels. *Top*: two shocks, propagating according to the arrows, induce transitions between zones $0 \rightarrow 1$ and between $1 \rightarrow 2$. *Middle panel*, the instance of collisions between the shocks. The transition $0 \rightarrow 2$ does not correspond to consistent shock jump conditions. *Bottom*: at the Lagrangian location of the collision an isobaric discontinuity between 3_o and 3_i forms, separating between a forward moving shock ($0 \rightarrow 3_o$) and a reflected rarefaction (smooth transition between 2 and 3_i).

shocks; adjacent to zone 0) and zone 3_i (inner; adjacent to 2), separated by the SICF. We refer to the plasma density, pressure, velocity and speed of sound respectively as ρ , p , u and c . Velocities of shocks at the boundaries between zones are denoted by v_i , with i the upstream zone. We rescale all parameters by the unshocked parameters ρ_0 and p_0 .

The velocity of the leading shock is

$$v_0 = u_0 + M_0 c_0, \quad (1)$$

where

$$c_i = \left(\frac{\gamma p_i}{\rho_i} \right)^{1/2} \quad (2)$$

for each zone i . Without loss of generality, we measure velocities with respect to zone 0, implying $u_0 = 0$.

The state of zone 1 is related to zone 0 by the Rankine-Hugoniot conditions,

$$p_1 = p_0 \frac{2\gamma M_0^2 - \gamma + 1}{\gamma + 1}, \quad (3)$$

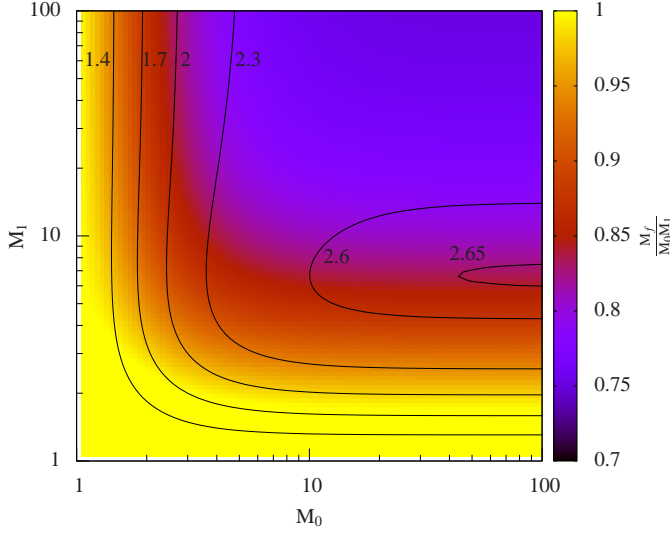


Figure 2. Contrast q (labeled contours) of a CF generated by a collision between two trailing shocks with Mach numbers M_0 and M_1 , for $\gamma = 5/3$. The color map shows the final Mach number M_f normalized by $M_0 M_1$.

$$u_1 = u_0 + \frac{p_1 - p_0}{\rho_0(v_0 - u_0)}, \quad (4)$$

$$\rho_1 = \rho_0 \frac{u_0 - v_0}{u_1 - v_0}. \quad (5)$$

The equations are ordered such that each equations uses only known variables from previous equations. The state of the doubly shocked region (zone 2) is related to zone 1 by reapplying equations 1- 5 with the subscripts 0, 1 replaced respectively by 1, 2, and M_0 replaced by M_1 .

Across the contact discontinuity that forms as the shocks collide (the SICF), the pressure and velocity are continuous but the density, temperature and entropy are not; the CF contrast is defined as $q \equiv \rho_{3i}/\rho_{3o}$. Regions 0 and 3_o are related by the Rankine-Hugoniot jump conditions across the newly formed shock,

$$p_3 = p_0 \frac{(\gamma + 1)\rho_{3o} - (\gamma - 1)\rho_0}{(\gamma + 1)\rho_0 - (\gamma - 1)\rho_{3o}}, \quad (6)$$

$$u_3 - u_0 = \left[(p_3 - p_0) \left(\frac{1}{\rho_0} - \frac{1}{\rho_{3o}} \right) \right]^{1/2}. \quad (7)$$

The adiabatic rarefaction from pressure p_2 down to $p_3 = p_{3i} = p_{3o}$ is determined by

$$u_2 - u_3 = -\frac{2c_2}{\gamma - 1} \left[1 - \left(\frac{p_3}{p_2} \right)^{(\gamma-1)/2\gamma} \right]. \quad (8)$$

The system can be solved by noting that the sum of eqs. (7) and (8) equals $u_2 - u_0$, fixing ρ_{3o} as all other parameters are known from eqs. (1-6).

Finally, the Mach number of the new shock and the rarefacted density are given by

$$M_f^2 = \frac{2\rho_{3o}/\rho_0}{(\gamma + 1) - (\gamma - 1)\rho_{3o}/\rho_0}, \quad (9)$$

$$\rho_{3i} = \rho_2(p_3/p_2)^{1/\gamma}. \quad (10)$$

Closed-form expressions for q and M_f are presented in § A. Figure 2 shows the discontinuity contrast q for vari-

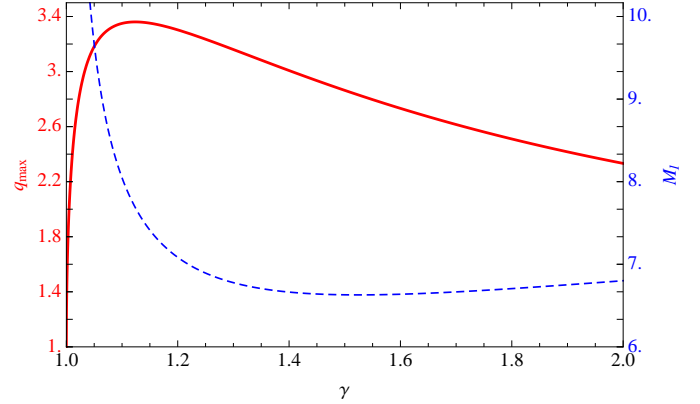


Figure 3. The maximal SICF contrast (solid, left axes) as a function of γ . It occurs in a collision between a very strong shock $M_0 \rightarrow \infty$ and a trailing shock of finite Mach number M_1 (dashed, right axes). For $\gamma = 5/3$, $q_{max} = 2.65$ with $M_1 = 6.65$.

ous values of M_0 and M_1 , for $\gamma = 5/3$. Typically $q \sim 2$, ranging from 1.45 for $M_0 = M_1 = 2$, for example, to $q_{max} = 2.653$. The figure colorscale shows the dimensionless factor $f \equiv M_f/(M_0 M_1)$, ranging between 0.75 and 1 for $1 < \{M_0, M_1\} < 100$.

The maximal contrast q_{max} depends only on the adiabatic index, as shown in fig. 3. It occurs for a very strong primary shock $M_0 \rightarrow \infty$ and a finite secondary M_1 ; see § A for details. For $\gamma = 5/3$ we find $q_{max} = 2.653$, achieved for $M_0 \gg 1$ and $M_1 \simeq 6.65$.

2.2 Planar Hydrodynamic Example of SICF Formation

To demonstrate the formation of an SICF we present in fig. 4 results from a 1D planar hydrodynamic code. The numerical scheme of the hydrodynamic calculation is Lagrangian, with the locations and velocities defined at edges of cells and thermodynamic variables defined at the centres of cells. The density ρ and internal energy e , are the free thermodynamic variables, setting the pressure p , temperature T and the entropy S according to an ideal gas equation of state. Throughout the paper we consider monoatomic gas, with an adiabatic constant of $\gamma = 5/3$ unless stated otherwise. The time propagation is calculated by a leap-frog explicit scheme. The timesteps here are adaptive, and set by a standard Courant Friedrichs Levy condition. Discontinuities are integrated over by employing first and second order Von Neumann artificial viscosity.

The simulation presented in fig. 4 was run with 500 cells. Without loss of generality, we can assume $\rho_0 = e_0 = T_0 = 1$. The definition of temperature here implies an arbitrary heat capacity that does not enter into the equations of motions. We define the entropy as $S \equiv T/\rho^{\gamma-1}$ (the exponent of the usual formal definition) so $S_0 = 1$ as well. We use external boundary conditions of a piston propagating into the material from $X = 0$ in the positive direction at Mach number $M_1 = 2.35$. At time $t = 0.04$ the piston's velocity is increased to create a second shock propagating in the same direction, with $M_2 = 1.76$ with respect to the previously shocked gas.

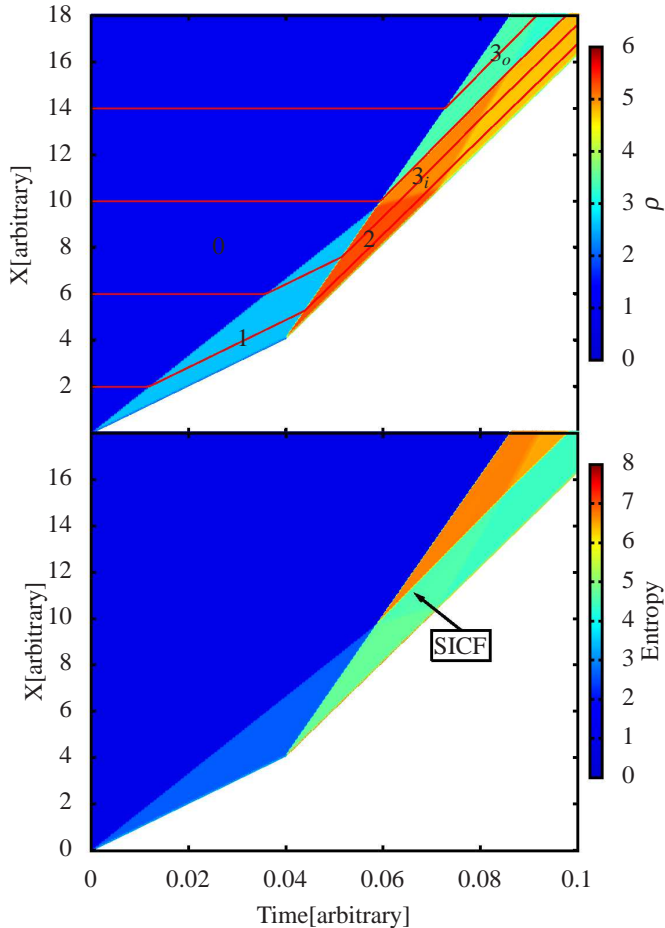


Figure 4. Shock tube simulation of a contact discontinuity (SICF) formed by merging of two shocks. The piston propagates from $x = 0$ in the positive direction at a supersonic speed creating the shock between $0 \rightarrow 1$. At $t=0.04$ the piston’s velocity abruptly increases causing a second shock to propagate between $1 \rightarrow 2$. At the position and time where the shocks merge a contact discontinuity forms between regions 3_o and 3_i . *Top:* density (normalized so that $\rho_0 = 1$). Red lines mark the trajectories of some Lagrangian cell boundaries. The zones here are analogous to those in § 2 and fig. 1. *Bottom:* entropy (normalized so that $S_0 \equiv T_0/\rho_0^{2/3} = 1$). Note that there is no entropy change between zone 2 and 3_i because the gas rarefies adiabatically between them. The contrast of the SICF, q , is the density jump between zones 3_o and 3_i .

The contact discontinuity that forms has a density ratio¹ $q \equiv \rho_{3i}/\rho_{3o} = 1.466$ while the theoretical prediction according to equations 1-10 is $q = 1.459$ - in satisfactory agreement for the resolution used, and for the accuracy needed in the discussion presented here. The same technique has also been performed for larger Mach numbers and yielded results with comparable accuracy.

¹ The SICF strength is calculated in the simulation according to $q = (S_{3i}/S_{3o})^{-1/\gamma}$ because in the rarefied zone, 3_i the density is not constant, and so harder to measure directly, while the entropy is constant throughout the zone.

3 NUMERICAL INVESTIGATION OF SPHERICAL COLD FRONTS

3.1 Driving Shocks

We explore different ways to drive central shocks through clusters of galaxies. The first, most intuitive method is external energy injection at the centre (i.e. explosions), which would correspond, for example, to mechanical energy released in AGN bursts. Observations in X-ray and radio indicate a wide variety of shocks and sound waves (Fabian et al. 2003; Forman et al. 2007) emitted repeatedly, perhaps even periodically from a central AGN. Many clusters also include hot and diffuse bubbles, that are most likely inflated by AGN jets that are decollimated by the ambient cluster gas (see review by McNamara & Nulsen 2007, and reference therein). If these bubbles are a plausible mechanism to counteract the overcooling problem, the energies associated with them must be comparable to the cooling rate of the clusters ($\gtrsim 10^{44} \text{erg sec}^{-1}$; Edge et al. 1990; David et al. 1993; Markevitch 1998) over some fraction of the Hubble time, indicating that the total energy injection is $\gtrsim 10^{61} \text{erg}$. The process of inflation of these bubbles sends shocks through the ICM, but at the same time the extremely hot, underdense bubbles alter the radial structure of the ICM in a non trivial manner. In § 4.1 we demonstrate (noting the limitations of the spherically symmetric analysis in that case) that mergers between shocks driven by such central explosions can produce SICFs.

Shocks can also be driven gravitationally. Mergers of galaxies and subhaloes change the structure and depth of the potential well causing sound waves and shocks to propagate through the haloes. These shocks typically do not considerably disturb the ICM structure, leaving a static gaseous halo after they propagate. We show in § 4.2 that abrupt changes to the gravitational potential of the halo directly produce shocks. In particular, in the first passage stage of a merger, two outward propagating shocks are produced: one when the halo contracts due to the increase of the gravitational force, and another when the halo abruptly rarefies once the merging subhalo flies out. The numerical investigation of explosion and merger driven SICF is performed using a spherical one dimensional hydrodynamic code within a static potential well (a version of the code “Hydra” documented in Birnboim & Dekel 2003, that is stripped from the dynamic dark matter evolution and self-gravitating gas) that, along with the initial conditions, is described in § 3.2.

In § 5 we investigate the interaction of a secondary shock with the virial shock that is always expected at edges of clusters. To produce this primary shock, we simulate the cosmological evolution of a cluster by using a hydrodynamic scheme that includes a self-gravitating gas that flows within self-gravitating, dynamic dark matter shells, and starts from spherical cosmological overdensities at a redshift $z = 100$. We show that perturbations can either be invoked manually, or occur naturally when infalling dark matter has sufficiently radial orbits so it interacts with the central core directly. In this context, we also show that low amplitude perturbations in the core send sound waves that can steepen into a shock that interacts with the virial shock.

3.2 The “Hydra” Hydrodynamical Code

The cosmological implications of shock interactions in clusters are tested using 1D, spherical hydrodynamic simulations performed with “Hydra” (Birnbom & Dekel 2003). The code is run here in two modes: cosmological and static DM (dark matter) modes. In § 4 we use the code in the static DM mode, a simplified configuration in which the baryons do not self-gravitate, and there is no evolution of the dark matter. Rather, baryons start in hydrostatic equilibrium within a fixed cluster-like potential well. In § 5 we use the code in its cosmological mode, utilizing the full capabilities of the code to evolve baryons and dark matter self-consistently from a cosmological initial perturbation at high redshift to $z = 0$. Next, we summarize the physical processes implemented in both modes of “Hydra” and then highlight the difference in boundary conditions and initial conditions corresponding to each modus operandi.

Similar to the planar code described in § 2.2, the code uses a Lagrangian scheme. The positions of baryonic spherical shells are defined by their boundaries (with the innermost boundary at $r = 0$), and the thermodynamic properties are defined at centres of shells. A summary of the fluid equations that are solved, and the numerical difference scheme is available in Birnbom & Dekel (2003). The code (in its cosmological mode) also evolves thin discrete dark matter shells, that propagate through the baryons, and interact with them gravitationally. The full discrete force equation for the “ i ”th baryonic shell is thus:

$$\ddot{r}_i = -4\pi r^2 \frac{\Delta P_i}{\Delta M_i} - \frac{GM_i}{(r_i + \epsilon)^2} + \frac{j_i^2}{r_i^3}, \quad (11)$$

with r_i, M_i, j_i the radius of boundary i , the mass (baryonic + DM) enclosed within that radius, and the specific angular momentum prescribed to this shell respectively, and $\Delta P_i, \Delta M_i$ the pressure difference and baryonic mass difference between the centres of shells $i + 1$ and i . ϵ is the gravitational smoothing length (50 pc and 500 pc in the static DM and cosmological modes respectively).

The dark matter and baryonic shells are assigned angular momentum that acts as an outward centrifugal force designed to repel shells that are close to the singularity at the centre, in analogy to the angular momentum of a single star, or of the gaseous or stellar disk in realistic systems, keeping them from falling into the centre of the potential well in the absence of pressure support. In the cosmological mode the shells are initially expanding with a modified Hubble expansion, and the angular momentum is added as each shell turns around, corresponding to the physical generation of angular momentum via tidal torquing around the maximal expansion radius. In the static DM mode, the angular momentum is present from the beginning of the simulation, and is taken into account when the hydrostatic initial profile is calculated. The angular momentum prescription of the baryons is determined by the requirement that as gas passes through the virial radius, its angular momentum will be some fraction ($\lambda = 0.05$, Bullock et al. 2001) of the value needed to support it on circular motions. As expected, the gas only becomes angular momentum supported near the centre, and when gas cooling is turned on (in the simulations presented below, the angular momentum of the baryons is never important, and is presented here only for

completeness). The dark matter is prescribed angular momentum according to the eccentricity of a shell’s trajectory as it falls in through the virial radius: $j = v_{\text{vir}} r_{\text{vir}} \sqrt{2(1 - \beta)}$, (corresponding to: $v_\theta^2 = v_\phi^2 = (1 - \beta)v_r^2$; Binney & Tremaine 1987, § 4.2). $v_{\text{vir}}, r_{\text{vir}}$ are the virial velocity and radius, and v_r, v_θ, v_ϕ are the radial and two tangential velocity components of an infalling trajectory. Low values of β indicate large angular momentum, and $\beta = 1$ corresponds to purely radial orbits. β is constant for all the dark matter shells in the simulation. Gas cooling can be turned on, by interpolating from a tabulated version of Sutherland & Dopita (1993), with a prescribed metallicity.

Rather than use a leap-frog integration scheme, which is sufficient for most explicit hydrodynamic schemes, we use here 4th order Runge-Kutta integration over the coupled dark matter and baryonic timestep. This allows us to derive a timestep criterion for the dark matter shells, by comparing changes in the velocities and radii of the dark matter and baryons between the 1st and 4th order propagation and limit this difference to some fraction of the velocity and radius. The timestep is determined by the combined Courant Friedrichs Levy condition and this requirement. If the criterion is not met, the code reverts to the beginning of the timestep and recalculates the next step with a reduced timestep.

The numerical integration scheme, angular momentum and cooling is described in Birnbom & Dekel (2003). In addition, we report here on two new ingredients to the calculation: adaptive changes to the grid, and 1D convective model. Baryonic shells are now split and merged if they become too thick or thin respectively. A shell is split if its width is larger than some fraction (typically 0.2) of its radius, or if it is larger than some fraction (typically 4) of the shell directly below it and above it, provided that it is larger than a minimal value (typically 2 kpc), and that the shell is not in the angular momentum supported region near the centre of the halo. Shells are merged when the cumulative width of two adjacent shells is smaller than some value (typically 0.1 kpc). Shell merging is helpful in cases where two shells are pressed together, decreasing the timestep to unreasonable values (reasonable timesteps for cosmological simulations are above 10^{-7} Gyr). An additional component included in “Hydra” for the first time is a 1D mixing length convection model, that acts to transfer energy outwards in regions where the entropy profile is non-monotonic (Spiegel 1963). This model is described in detail in Birnbom & Dekel (2010), and is used here only in the final case described in § 5 in its maximal form: bubbles can rise until they reach the local speed of sound. In this work, the inclusion of the maximally efficient mixing length theory convection ensures that the entropy is always monotonically increasing, in an energetically self-consistent way.

The initial conditions for a cosmological run are derived by requiring an average mass evolution history for a halo with some final mass (Neistein et al. 2006). The overdensity of each shell at the initial time is calculated so that the shell would pass through its virial (r_{180}) radius at the required time (the procedure is described in detail in Birnbom et al. 2007). This procedure has an additional benefit of setting the initial grid in a way that would ensure that shells will pass through the virial radius at constant time intervals. In this procedure, and in the cosmological simulation, a force

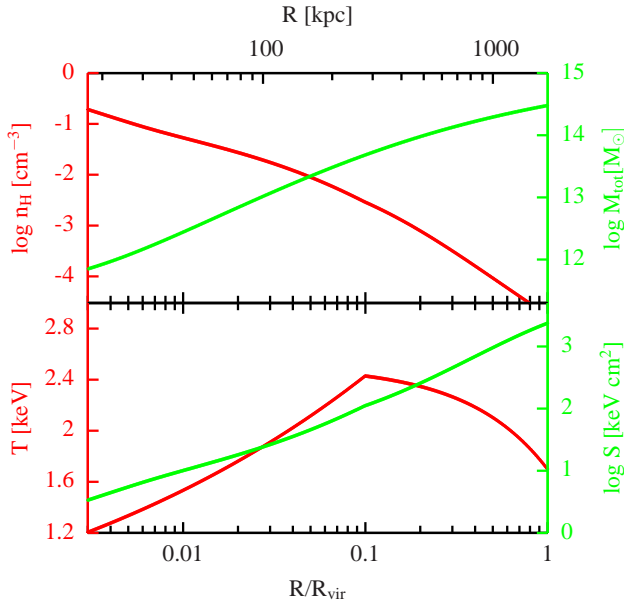


Figure 5. Radial profiles of cluster initial conditions. *Top:* density (red, left axis) and total enclosed mass (green, right axis) of the cluster. *Bottom:* Temperature (red, left axis) and entropy (green, right axis), as a function of radius (upper x axis) and virial fraction (lower x axis). The total mass profile, and the temperature profile are prescribed, as well as a pivot point in the entropy (value of 10 keV cm^2 at $r = 0.01 R_{\text{vir}}$). The density and entropy profiles are calculated so that the gas is in hydrostatic equilibrium. The temperature profile is set to exhibit a decrease by a factor ≈ 1.5 between 0.1 to $0.01 R_{\text{vir}}$.

corresponding to the cosmological constant has been added to eq. 11, making the simulation completely consistent with Λ CDM (Birnboim et al. 2007) (the cosmological parameters used throughout the paper are: $\Omega_m = 0.3$, $\Omega_\Lambda = 0.7$, $h = 0.7$). This has little overall effect, and essentially no impact once the shells are collapsed, and the overdensities become non-linear.

In the stripped down, static DM mode, there are no dark matter shells, and the gas does not self-gravitate. Instead, the value M_i of eq. 11 is interpolated from a predefined lookup table. In this mode, a rigid external boundary condition is applied, in contrast to a vacuum boundary condition in the cosmological mode. The inner boundary condition in both cases is trivially satisfied because all terms in eq. 11 are individually zero there.

For the static DM simulations we wish to define initial conditions which are typical of those in clusters. The total mass profile is defined by an NFW profile (Navarro et al. 1997), with $M_{\text{vir}} = 3 \times 10^{14} M_\odot$, and concentration set to $c = 5.4$ according to Bullock et al. (2001). The virial radius is 1730 kpc. A central galaxy (BCG) is modeled by a Hernquist profile (Hernquist 1990) superimposed on the NFW profile, with a sharp cutoff at 10 kpc and concentration $a = 6$ kpc normalized to $M_{\text{BCG}} = 3 \times 10^{11} M_\odot$. We define an inward decreasing temperature profile (Leccardi & Molendi 2008) that peaks at $r_T = 0.1 R_{\text{vir}}$ at $T(r_T) = T_{\text{vir}} = 2.7 \times 10^7 \text{ K}$ and drops inwards according to $T(r) = T_{\text{vir}}(r/r_T)^{0.2}$. Outwards, it is linearly decreasing from $T(r_T) = T_{\text{vir}}$ to $T(R_{\text{vir}}) = 0.7 T_{\text{vir}}$. Once the entropy of a single point is defined, the density profile can be

constructed by the hydrostatic requirement without further degeneracy. We set $S(0.01 R_{\text{vir}}) = 10 \text{ keV cm}^2$ as our pivot point (Cavagnolo et al. 2009). The final baryonic mass of the resulting profile in the ICM is $2.5 \times 10^{13} M_\odot$, which is $\approx 8\%$ of the total mass. The density, total mass, temperature and entropy profiles are plotted in fig. 5. We note that while the constructed initial profile reasonably resembles that of a realistic cluster, the mechanism that is studied here, of SICFs, is not sensitive to these details; any merging between shocks, in any profile, should produce them.

4 STATIC DM SIMULATIONS

4.1 Cluster Explosions

The first mechanism we investigate to produce shocks is that of cosmic explosions. Many processes can cause abrupt energy injection at centres of clusters, among which are AGNs or starbursts at the BCG and galaxy-galaxy mergers. The discussion in this section is confined to injection to the baryonic component itself (changes to the gravitational potential well will be discussed next). As shocks sweep through matter, they constantly loose energy to heating the gas, and when the shocks expand spherically, they also weaken due to the geometrical increase in the surface of the shock². We seek here to create shocks that will survive to some considerable fraction of the halo radius, requiring that the amount of energy that is injected will be comparable to the total thermal energy of the gas in the cluster. This energy scale is similar to that required to solve the overcooling problem, indicating that any solution to the cluster overcooling problem via strong shocks will produce shocks that will expand to a significant fraction of the halo radius.

Fig. 6 describes the time dependent evolution of an initially hydrostatic cluster atmosphere, as two explosions are driven through it. The simulation has 1,000 logarithmically spaced shells, between $0.0005 R_{\text{vir}}$ and R_{vir} . Here, and in the following examples, the cooling is turned off, which is justified in the absence of any feedback mechanism in the simulation that would counteract the overcooling. The explosions are driven by setting a homologous ($v = v_{\text{exp}} r / r_{\text{exp}}$) velocity profile with highly a supersonic velocity (v_{exp}), sharply cutting off beyond some radius r_{exp} . For the first explosion, these parameters are $v_{\text{exp}} = 10,000 \text{ km sec}^{-1}$ and $r_{\text{exp}} = 20 \text{ kpc}$, injecting $1.7 \times 10^{61} \text{ erg}$ into the core of the cluster. The second explosion, $3 \times 10^7 \text{ yr}$ later, has a velocity of $v_{\text{exp}} = 20,000 \text{ km sec}^{-1}$ at $r_{\text{exp}} = 40 \text{ kpc}$, and injects $4.7 \times 10^{61} \text{ erg}$. These large values are not atypical for the energy estimated in radio bubbles (Birzan et al. 2004; McNamara & Nulsen 2007). While no buoyancy is possible within a spherical symmetric framework, the explosions do create extremely hot and dilute regions, and drive strong shocks. The two shocks can be traced in fig. 6 by the breaks in the plotted Lagrangian lines (velocity jump), by the temperature jump, and by the regions in the simulation with large artificial viscosity (black dots). At the location of

² Waxman & Shvarts (1993); Kushnir et al. (2005) showed that for power law density profiles and strong shocks, as long as the mass diverges with radius, or, $\rho_{\text{gas}} \propto r^{-w}$, with $w \leq 3$, the shock will weaken

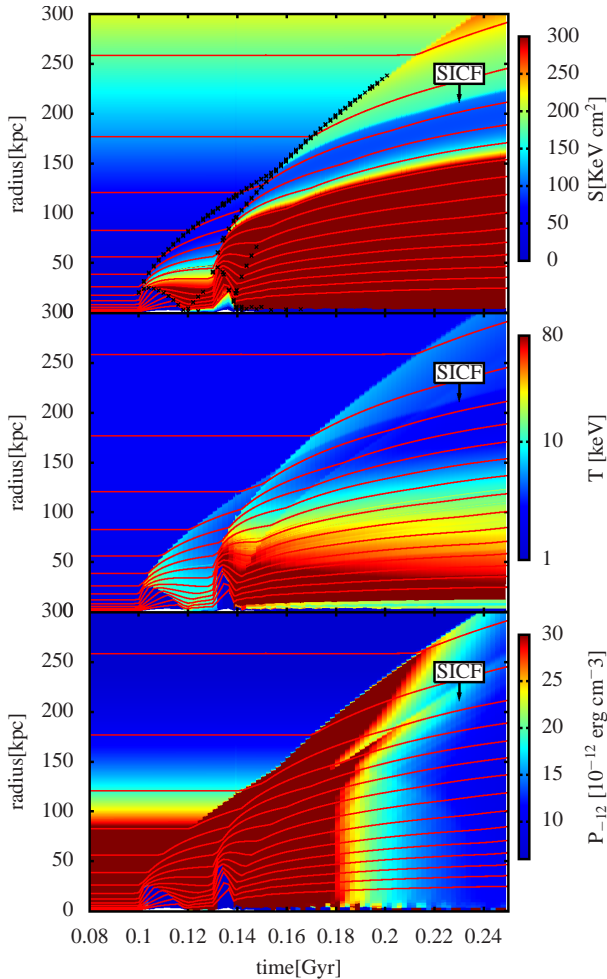


Figure 6. Time evolution of an initially hydrostatic halo showing explosion driven shocks from the centre propagating outwards. The energy injection parameters are described in the text. *Top:* entropy color map on the radius-time plane. The red thin lines mark the position of every 50th Lagrangian shell boundary. The black dots mark shocks, defined as artificial viscosity pressure exceeding $10^{-11} \text{ erg cm}^{-3}$. These shocks are driven by two explosions, at $t = 0.1$ Gyr and 0.13 Gyr. The entropy of the shocked gas is saturated in this colormap, but the entropy jump of the SICF is visible at the Lagrangian location of collision between the shocks. *middle:* temperature colormap of the same simulation. The temperature increase induced by the shocks, and the temperature jump at the SICF (by a factor of 1.3) is visible. *Bottom:* Pressure colormap. The pressure across the SICF is smooth, as expected for cold fronts.

merging between the shocks (at $t = 0.15$ Gyr and radius ≈ 150 kpc), an SICF (contact discontinuity) forms (visible in the entropy colormap) that propagates with the matter. We have followed the simulation for 1 Gyr and, as expected in the absence of any diffusive mechanisms, the SICF retains its strength.

The energies and time interval between the shocks have been chosen arbitrarily to create a shock collision at ≈ 150 kpc. A series of sharp, frequent and strong central shocks is expected in some self-consistent radiative and mechanical AGN feedback models (Ciotti & Ostriker 2007; Ciotti et al. 2009), and is indicated in some observations

(for example, Fabian et al. 2003; Forman et al. 2005, for Perseus and M87 respectively). Non-spherical, frequent collisions may occur between the shocks produced by the two bubbles of a radio active AGN, at a position roughly above one of the bubbles (the generation of two shocks corresponding to observed bubbles, as well as radial soundwaves that steepen into a shock is discussed in Fabian et al. 2003). The shock from the near-by bubble (primary) arrives to that position first, and the shock from the opposite bubble (secondary) arrives later. Given our 1D framework, we do not attempt to map the parameter space of possible explosions. Since shocks weaken as they propagate outwards, weaker shocks which occur within a shorter time interval will produce smaller radii SICF with the same strength as stronger shocks driven within a larger time interval.

4.2 Gravitational Perturbations: Merger Induced Shocks

If the core of an otherwise hydrostatic cluster is gravitationally perturbed, the reaction of the gas to the perturbation often results in shocks. While explosions, discussed in § 4.1, typically considerably heat the shocked gas near the centre, gravitational perturbations make a more subtle change to the gas, while forming strong outward expanding shocks. The core is perturbed when gas or dark matter is accreted to the centre of the cluster, either smoothly (creating weak perturbations) or by mergers, (causing a more violent and abrupt shock). In this section we describe the shocks that occur as a result of a large change to the core potential depth of a cluster due to mergers. In § 5 we show that weak oscillations in the core send sound waves through the gas, that steepen into shocks.

Fig. 7 shows a merger event of a cluster with the same initial conditions described in § 3.2 and fig. 5 with a dense substructure with total mass of $3 \times 10^{13} M_{\odot}$ (a 10:1 merger ratio). The simulation describes, in a simplified form, how the main halo will react to the first passage of the substructure near its core. During its first pericenter passage, the subcluster will first cause the core to contract, and then, as it flies out, allow the core to relax again. Here, we model this in a simplistic way by adding, and then removing (after 2×10^7 yr), a massive object at the centre of the simulated cluster. The addition of the mass causes all the cluster’s atmosphere to contract, affecting the inner region more than the outer. A coherent flow inwards begins, that stops as an outward expanding shock passes through the cluster, readjusting it to a new hydrostatic equilibrium (note in fig. 7 that after the passage of the primary shock the post-shock gas is almost at rest). Once the central object is removed, the halo jolts out from the inside out (again, because the addition of the central force affects the inner core the most), causing another shock to occur. The energy for these two shocks is taken from the orbital energy of the merging subcluster, and would cause it to spiral in. In the figure both shocks are clearly visible in the temperature maps, and through the black dots corresponding to strong artificial viscosity. At the instant of merging between the shocks (at $t = 0.044$ Gyr and radius ≈ 25 kpc), an SICF forms which is seen in the entropy and temperature colormaps. The time interval for the merger interaction is chosen manually, but does not seem improbable noting that an object approaching the centre

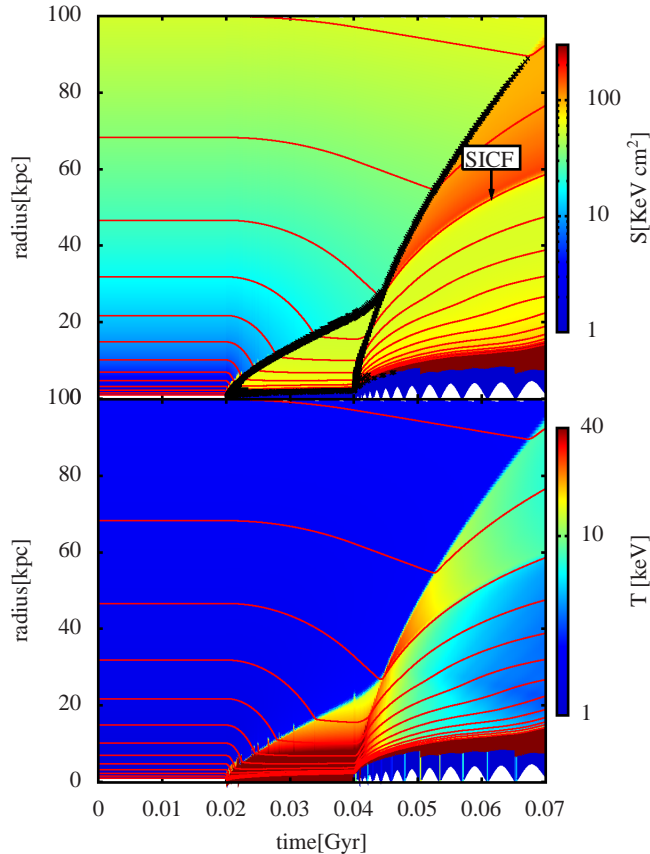


Figure 7. Same as fig. 6, but now the potential well is modified by artificially adding a central object of mass $3 \times 10^{13} M_{\odot}$, which is then removed 2×10^7 yr later (corresponding to a first passage of a 1:10 ratio subhalo). Note that the scales are different from fig. 6.

at 1000 km sec^{-1} , roughly the virial velocity, passes 20 kpc during that period. Shocks associated with sequential core-passages of an inspiraling subhalo could also induce large scale SICFs. While shocks produced by merger events have been seen in simulations (McCarthy et al. 2007), the formation of SICF in these simulations hasn’t been tested yet, and is left for future work.

5 VIRIAL SHOCKS AND SICFS

At the edges of galaxy clusters there are virial shocks with typical Mach numbers $\sim 30 - 100$, heating the gas from $\sim 10^4 \text{ K}$ to $\sim 10^7 \text{ K}$ by converting kinetic energy into thermal energy. Virial shocks are probably observed by Suzaku (George et al. 2009; Hoshino et al. 2010). The rate of expansion of a virial shock is set on average by the mass flux and velocity of the infalling material (see for example Bertschinger 1985). Secondary shocks that originate from the centre of clusters, due, for example, to the mechanisms discussed in § 3 will collide and merge with the virial shock, creating SICFs at the locations of the virial shock at the corresponding times. Since shock mergers with virial shocks require only one additional shock to form (rather than two in the general cases described in § 4), and no particular

timing is required, such SICFs are perhaps even more probable. When the Mach number of the primary (virial) shock is $M_0 \gtrsim 3$, which is always the case, the strength of the SICF becomes almost independent of the secondary shock, allowing for a rather narrow range of strengths around $q \approx 2$ as long as the secondary shock is sufficiently strong (fig. 2).

We simulate the merging of a virial shock with a secondary by evolving self consistently the dark matter and baryons from an initial perturbation in the cosmological mode described in § 3.2. These initial conditions provide a reasonable laboratory for gas dynamics in the ICM, producing correct temperatures and densities, and tracking the virialization process of the gas in a self consistent way. In order to capture the production of a secondary shock and its interaction with the virial shock in 1D simulation, we examine various artificial schemes which mimic the full 3D dynamics, as discussed below. A more detailed simulation of cluster evolution would require 3D simulations that include AGN feedback and merger and smooth accretion for baryons and dark matter. The cosmological simulations here have been performed with 2,000 baryonic shells, and 10,000 dark matter shells, sufficient according to our convergence tests.

For the average mass accretion histories used here (§ 3.2), the accretion rate grows with halo mass, even after taking into account the late time decline in accretion rates (Dekel et al. 2009), so shells that fall later are more massive. When late massive dark matter shells fall into the inner core, their mass becomes comparable to that of the gas enclosed within that shell, causing it to vibrate stochastically. These core vibrations drive sound waves that are emitted from the centre and steepen to create shocks (the energy for these shock is taken from the orbits of the dark matter shells). We can control the level of stochastic noise by increasing or decreasing the angular momentum prescribed to the dark matter. In the first two “synthetic” examples shown here, we use $\beta = 0.7$ (see § 3.2) to reduce noise in the evolution, and then manually add perturbations at time -7 Gyr ($z = 0.84$). In the last example, we decrease the dark matter angular momentum ($\beta = 0.991$), and use the numerical stochastic noise as a proxy for the perturbations that halo cores undergo during their formation and accretion. We demonstrate that this noise naturally give rise to shocks that interact with the virial shock. This interaction seems to be quasi periodic, and we suggest a mechanism for driving this behavior. In this final example, the entropy profile is sometimes non-monotonic, implying that convection might be important. We test the effect of convection using our 1D mixing length theory and show that it does not significantly reduce the strength of the SICFs that are produced, and does not change the overall evolution significantly.

5.1 Manual Initiation of Secondary Shocks

Fig. 8 describes a typical evolution of a cluster that ends up with mass $3 \times 10^{14} M_{\odot}$ at $z = 0$, and subsequent interaction of the virial shock with a secondary merger induced shock. The merger here is 10:1, with a central mass of $3 \times 10^{13} M_{\odot}$ instantaneously added at -7 Gyr (at that time the cluster’s virial mass is $\approx 10^{14} M_{\odot}$). Unlike the procedure described in § 4.2, we do not remove the merged mass, creating only one

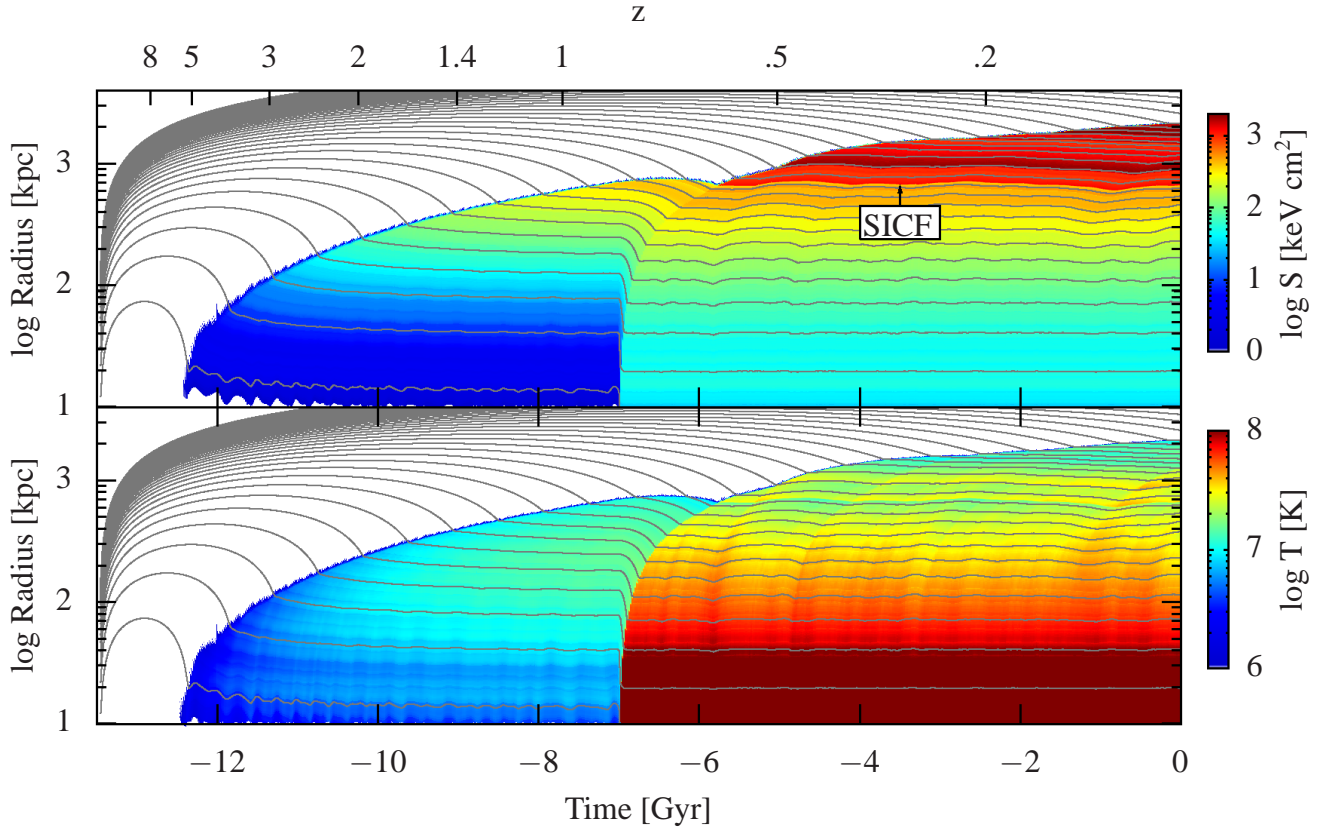


Figure 8. Cosmological mode simulation of the evolution of a $M(z=0) = 3 \times 10^{14} M_{\odot}$ cluster. The gray lines mark the evolution of every 50th Lagrangian shell, and the colormaps are entropy (*top*) and temperature (*bottom*). The initial Hubble expansion, turnaround and the virial shock are visible. Initially, at $z = 100$, shells expand due to the near-Hubble flow. At time -7 Gyr a central object with mass $3 \times 10^{13} M_{\odot}$ is permanently added, causing a shock to propagate outwards. The collision between this shock and the virial shock creates an SICF visible in the entropy colormap which persists to $z = 0$.

shock. The Hubble expansion, turnaround and virial shocks are seen, as well as the SICF formation at time ≈ -5.5 Gyr and at radius ≈ 700 kpc. After the deepening of the gravitational potential well, the secondary shock mediates the re-establishment of hydrostatic equilibrium. Thus, the post-shock gas, and the SICF, are roughly at rest in the Eulerian laboratory frame of reference. The post-shock temperatures, particularly below 100 kpc are unrealistically high, corresponding, perhaps, to disturbed morphologies seen in cluster merger events (the bullet cluster; Tucker et al. 1998), although no entropy inversion occurs there. This is remedied somewhat when the shock is initiated by a series of weaker shocks and sound waves that steepen into a strong shock further from the cluster’s centre (fig. 9), and is completely alleviated when the shocks are due to persistent stochastic noise near the core (§ 5.2), generating profiles which are also consistent with quiescent cool core clusters.

We produce a weaker, more local perturbation by engineering a perturber that sends weak shocks and sound waves that steepen into a shock. Fig. 9 shows an evolution of the same cluster as in fig. 8, but with a central perturber who’s mass is sinusoidally changing between $-7 < t < -6.75$ Gyr with an amplitude of $3 \times 10^{13} M_{\odot}$ and a period of of 5×10^7 Gyr. After that, a constant mass of $5 \times 10^{12} M_{\odot}$ is left. The steepening of the shocks is visible, and the temperature increase of the gas by the secondary

is much smaller, because, contrary to the permanent mass addition in fig. 8, no net contraction is caused. This example serves to show how shocks can form from “noise” generated near the core, but still heat the centre from the inside out, in a way that would correspond to a merger event but not to a quiescent cool core cluster. The entropy profile here becomes non-monotonic near the centre.

5.2 Self Consistent Initiation of Secondary Shocks

We allow numerical noise to perturb our hydrodynamic simulation by reducing the angular momentum of dark matter so that late infalling, massive dark matter shells penetrate the cluster core. The resulting time evolution and final profile are shown in figures 10 - 12. As soon as the cluster progenitor forms, at high redshift, sound waves and weak shocks begin propagating through the cluster, as the gas constantly adjusts to the varying potential well near the centre. The weak shocks steepen and accumulate to create strong shocks that propagate outwards and merge with the virial shock, creating an SICF on each merger instance. From fig. 10 it is evident that the shocks are weak, and that they do not alter the inner profile considerably.

The shocks that are invoked by the stochastic noise seem to be periodic, with a period corresponding to about twice the sound (or shock) crossing time through the cluster.

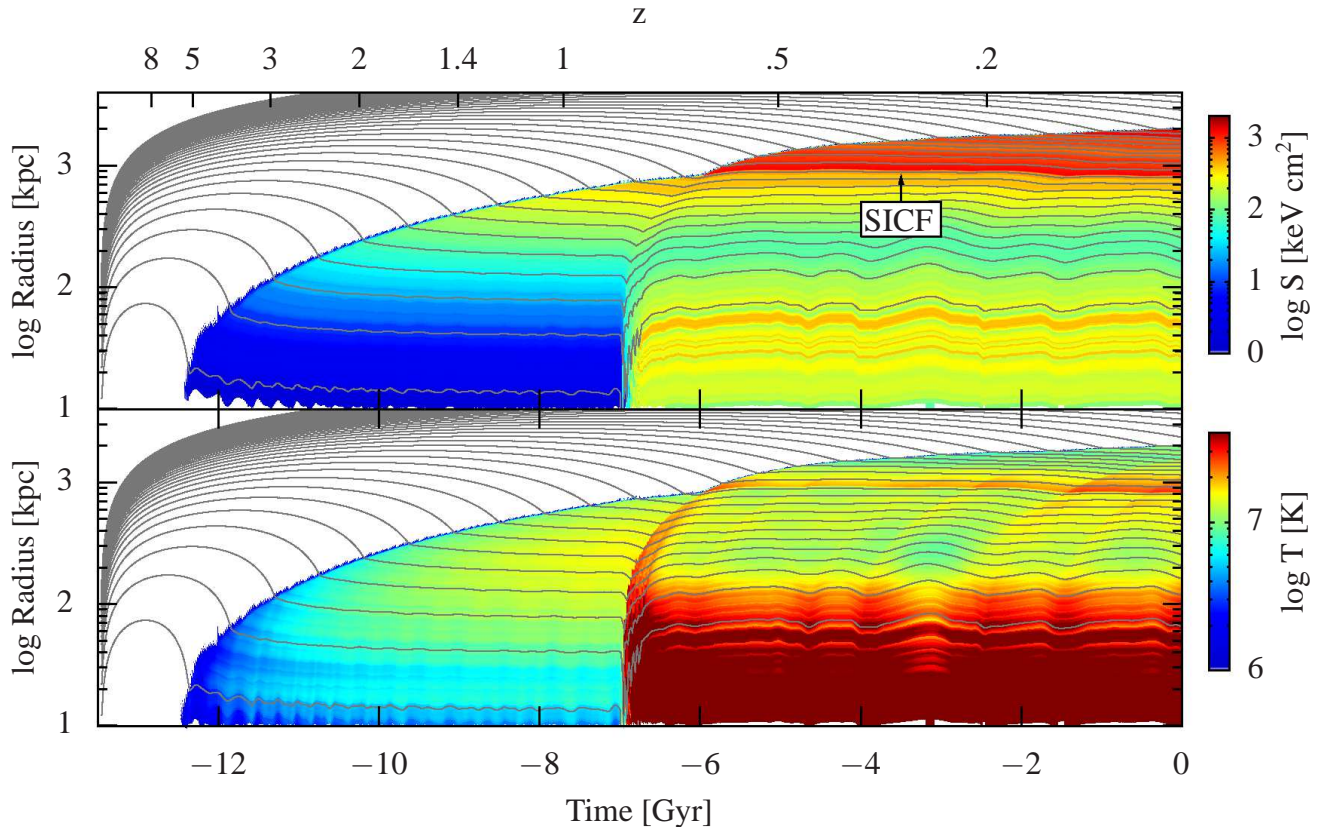


Figure 9. A cosmological mode simulation with the same initial conditions as in fig. 8, but with the core perturbed briefly between -7 and -6.75 Gyr (see § 5.1 for details). The perturbation is a sinusoid in time, with an amplitude of $3 \times 10^{13} M_{\odot}$, and a period of 5×10^7 Gyr, following by a constant left-over mass of $5 \times 10^{12} M_{\odot}$. Weak shocks and sound waves are sent outwards, steepening into a single shock that collides with the virial shock, producing an SICF.

Lacking a formal analysis for this oscillatory mode, we suggest, based on these simulations, the following explanation. The location of the virial shock is regulated such that the pressure below (towards the cluster’s centre) will support the shock and the ram pressure of the infalling gas (Bertschinger 1985). While this process would imply a smooth expansion of the shock, the virial shock can oscillate around its steady state trajectory in response to perturbations in the halo. When the post-shock gas is over-pressurized, the virial shock adjusts itself by expanding faster, relaxing this overpressure. If the relaxation overshoots, the pressure would drop below its steady state value, causing the shock to decelerate. The halo thus oscillates between these two phases depending on the virial shock’s velocity: in one it is overly slow, producing pressurization of the post-shock gas, and in the other it is overly fast, causing rarefaction. These modes are inter-laced. A rarefaction cycle begins with the secondary hitting the virial shock sending rarefaction waves inwards that are reflected at the centre and propagate outwards, ultimately reaching the virial shock making it decelerate. A compression, or secondary shock cycle collects compression waves that are transmitted inwards when the virial shock is too slow, and are reflected through the centre, ultimately steepening into what would become the secondary shock. Circumstantial evidence for this mode can be seen in fig. 11 where the shocks are automatically traced, and the trajectory of one rarefaction wave reflected from a secondary-virial shock

merger is highlighted by hand (dashed curve, based on a high resolution time sequence). Note that this periodicity is also seen (albeit much more weakly) in the two manual excitations of a secondary shock described in figures 8 and 9. The periodic SICFs that are produced can be seen in the entropy profiles in the upper panel of fig. 10, in the lines marking the gradient of the entropy in fig. 11, and in the final profile of this simulation shown in fig. 12. The shocks and rarefactions propagating through the halo, and the alternating speed of the virial shock³ are observed in the 3D galactic halo simulations of Kereš & Hernquist (2009)⁴. Note that this qualitative argument is similar to the one described in § 2. The overpressure there is caused by a secondary shock that perturbs the equilibrium solution of a single shock: the primary accelerates, and a rarefaction is sent back, relaxing the gas.

The calculations presented in Figures 10-12 are adiabatic. When cooling is turned on, and in the absence of

³ A movie of the evolution of radial profiles in time is available at <http://www.cfa.harvard.edu/~ybirnboi/SICF/sicf.html>

⁴ Dušan Kereš, (private communication). Propagation of merger induced shocks and the subsequent bounce of the virial shock as these secondaries merge with it are seen in http://www.cfa.harvard.edu/~dkeres/movies/B1hr_10n128_large_gas.mp4. There, left panel is gas density, right panel temperature, and a particularly notable shock forms at $z \approx 1.7$.

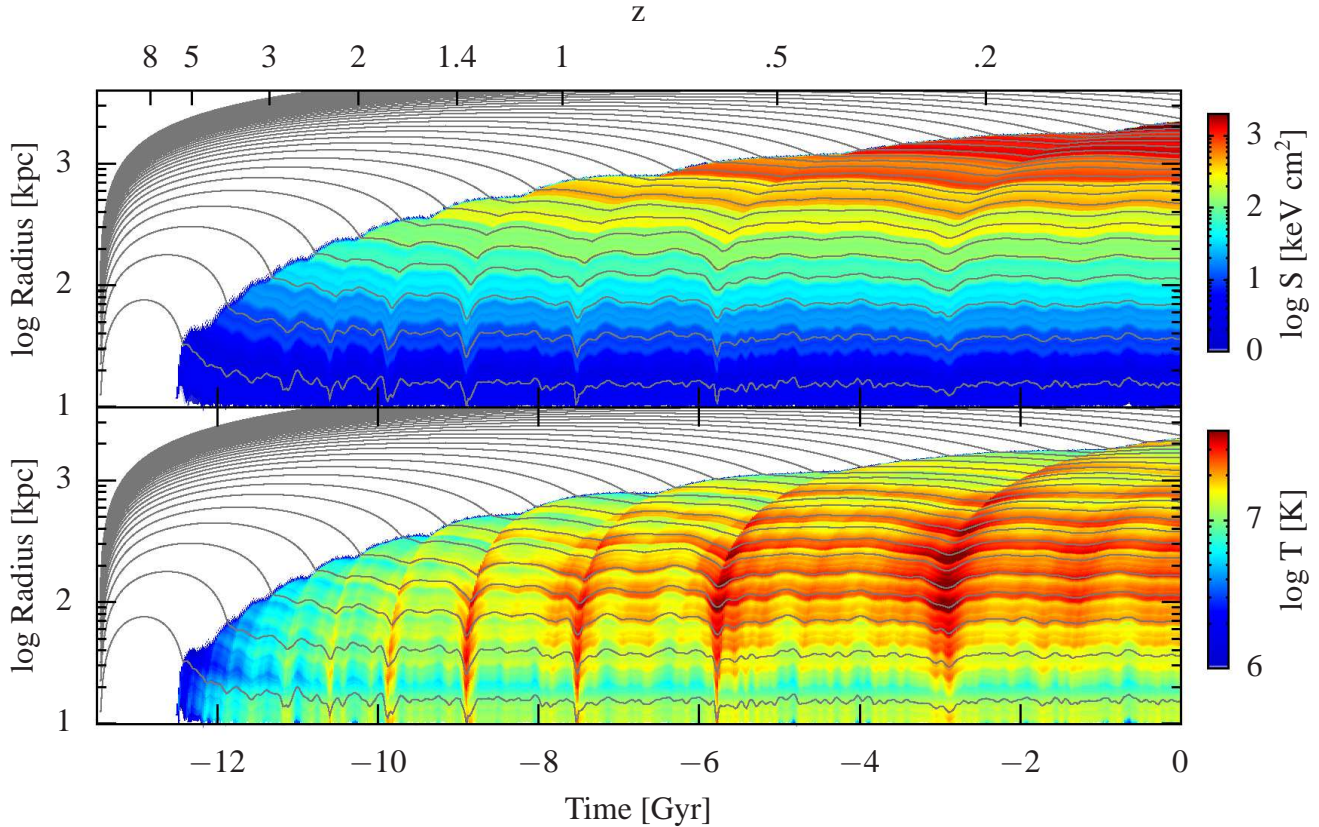


Figure 10. A cosmological mode adiabatic simulation of cluster evolution with initial conditions as described in the § 5.2. The angular momentum of the dark matter is sufficiently small to allow massive, late accretion of dark matter shells to propagate and reach the centre, increasing the amount of stochastic “noise” with respect to the levels seen in figures 8 and 9. A series of secondary shocks merge with the virial shock, creating a series of SICFs.

feedback, this simulation suffers from overcooling, creating an overmassive BCG of $2 \times 10^{12} M_{\odot}$ and BCG accretion rates (corresponding to star formation rates) of $\gtrsim 100 M_{\odot} \text{yr}^{-1}$, and the luminosity exceeds the $L_x - T$ relation (Edge et al. 1990; David et al. 1993; Markevitch 1998). The excitation of the basic mode, and periodic CFs, are observed in all these simulations. Since the virial shock’s strength is non-monotonic, it is not surprising that between SICF formation, the post-shock entropy is non-monotonic. This introduces a problem in 1D simulations where convection due to entropy inversion cannot naturally occur. We test this by rerunning the adiabatic simulation with 1D convection according to mixing length theory (Spiegel 1963), with the mixing length coefficient set such that the convection is limited only by the requirement that bubbles never exceed the sonic speed. This acts to redistribute the energy and entropy between SICFs, but does not change the overall dynamics. The final profile in this case is plotted in the dashed lines of fig. 12. The strength of the SICF in this case is reduced, but it is still clearly visible, with typical values of $q \approx 1.5$. It is highly improbable that convection operates in its maximal physical efficiency, particularly in the presence of ICM magnetic fields. Parrish et al. (2008, 2009) show that in the presence of weak magnetic fields the effective convection is smaller by many orders of magnitude than the heat fluxes carried by conduction, implying that it is highly suppressed from its

mixing length theoretical value (Ian Parrish, private communication).

We note a qualitative similarity between reverberations of the virial accretion shocks discussed here, and another prominent case of accretion shocks in astrophysics - of type II core collapse supernovae. Burrows et al. (2007) find that stalled accretion shocks around type II cores are unstable to 2D (g-mode) reverberation that, after enough cycles, accumulate sufficient energy and amplitude to cause an outbreak of the stalled shock. While the standing accretion shock instability (SASI) is predominantly 2D, and acts on different scales than discussed here, it does draw its energy from the accreted gas, and is perturbed by sound waves that are emitted from the vibrating core, that accumulate to a single unstable mode.

6 STABILITY AND OBSERVABILITY OF SHOCK INDUCED COLD FRONTS

6.1 Stability

The stability of CFs limits the time duration over which they are detectable, and so is important when comparing CF formation models with observations. Various processes can cause a gradual breakup or smearing of the CF. They act in other CF formation models as well.

Thermal conduction and diffusion of particles across

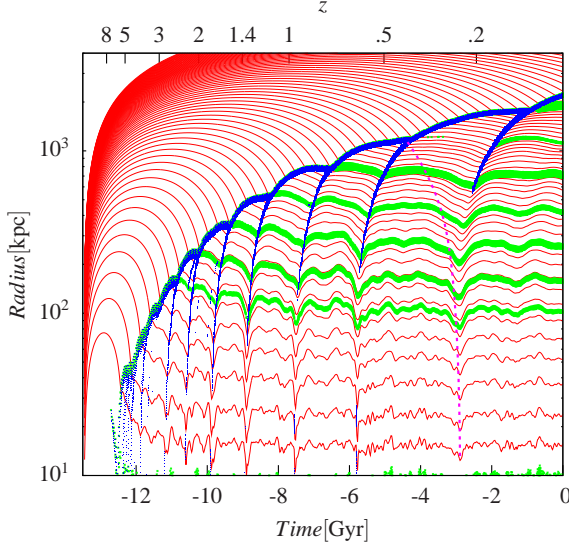


Figure 11. Evolution of a galaxy cluster from cosmological initial perturbations. The final mass of the cluster at $z = 0$ is $3 \times 10^{14} M_{\odot}$. The radius and time of Lagrangian shells (every 25^{th} shell) are plotted in red thin lines. Shocks are traced by large Lagrangian derivatives of the entropy ($d \ln S / dt > .1 \text{ Gyr}^{-1}$, blue dots), and CFs are traced by their large entropy gradients ($\partial \ln S / \partial \ln r > 0.5$, green dots). Rarefaction waves can be seen as small motions of the Lagrangian shells (illustrated by the dashed magenta curve, manually added based on a time series analysis). Their trajectory is approximately the reflection of the preceding outgoing compression, time inverted about the last secondary-virial shock collision.

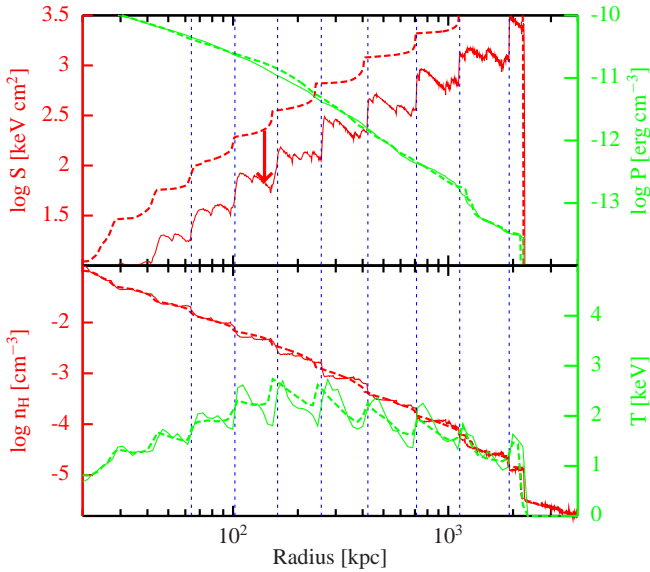


Figure 12. Thermodynamic profile of the simulated cluster shown in figures 10-11 at $z = 0$ (solid lines) and of the same simulation with maximal convection (dashed lines). *Top:* entropy (red, left axis) and pressure (green, right axis). The entropy of the convective simulation has been raised by 0.5 dec to distinguish between the models. *Bottom:* density (red, left axis) and temperature (green, right axis). The positions of CFs in the adiabatic, non-convective simulations are marked with blue dashed vertical lines.

the CF smears the discontinuity on a timescale that is set by the thermal velocity and the mean free path of the protons. The Spitzer m.f.p. λ in an unmagnetized plasma with typical cluster densities is a few kpc, and depends on the thermal conditions on both sides of the discontinuity (Markevitch & Vikhlinin 2007). Taking $\lambda \sim 10 \text{ kpc}$ and a thermal velocity $\bar{v} \sim 1000 \text{ km sec}^{-1}$, and assuming that a CF is visible if it is sharper than $L_{\text{obs}} \sim 10 \text{ kpc}$, we get a characteristic timescale for CF dissipation,

$$t \sim \frac{L_{\text{obs}}^2}{D} \sim \frac{3L_{\text{obs}}^2}{\bar{v}\lambda} \sim 10^7 \text{ yr.} \quad (12)$$

This result indicates that in order for shock induced CFs to be observable, either (i) they are formed frequently (e.g., by a series of AGN bursts; see Ciotti & Ostriker 2007; Ciotti et al. 2009); or (ii) magnetic fields reduce the m.f.p. considerably, as some evidence suggests (see the discussion in Lazarian 2006).

Heat flux driven buoyancy instability (HBI; Parrish & Quataert 2008; Quataert 2008; Parrish et al. 2009) tends to preferentially align magnetic fields perpendicular to the heat flow in regions where the temperature decreases in the direction of gravity. This effect has been argued to reduce radial diffusion within the inward cooling regions in the cores of cool core clusters. As suggested in Parrish & Quataert (2008), the temperature gradient across a CF is opposite to the direction of gravity, and HBI instability is expected to quickly form there (over 8 Myr in their example), aligning the magnetic fields parallel to the discontinuity and diminishing radial diffusion. This possibility needs to be addressed further by detailed numerical magneto-hydrodynamic simulations. Also, the timescale for achieving local thermal equilibrium between the electrons and ions below the virial shocks are long. It is unclear what the proper diffusion coefficients are in that case, and a particle transport analysis needs to be applied. These important issues are left for future work.

CFs could also be degraded by subsequent shocks that sweep outwards across the CF. This is true regardless of their formation mechanisms. However, the CF contrast is only slightly diminished by this effect. This is shown analytically by recalculating the Riemann problem described in § 2 but starting from a general contact discontinuity with strength q instead of a primary shock. For $q = 2$ this decrement is between 4% for $M_1 < 2$, to 20% for $M_1 \gtrsim 10$, as shown in fig. 13. Such passing shocks seed Richtmyer-Meshkov instabilities which could cause the CF to break down. Although less efficient than Rayleigh-Taylor instabilities, these instabilities operate regardless of the alignment with gravity. The outcome depends on M_1 and on any initial small perturbations in the CF surface. However, the instability is suppressed if the CF becomes sufficiently smoothed.

It is worth noting that KHI, which could break down CFs formed through ram pressure stripping and sloshing, does not play an important role in SICFs because there is little or no shear velocity across them. However, the stabilizing alignment of magnetic fields caused by such shear (Markevitch & Vikhlinin 2007; Keshet et al. 2009) is also not expected here.

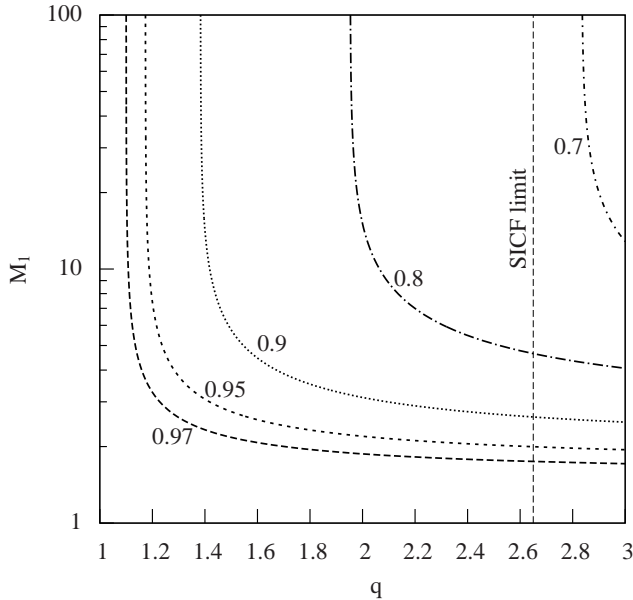


Figure 13. Fractional decline (contours) in initial CF contrast q induced by a collision with a shock of Mach number M_1 arriving from the dense CF side, for $\gamma = 5/3$. The vertical dashed line corresponds to the maximal SICF contrast, q_{max} .

6.2 Observability

Owers et al. (2009) present high quality Chandra observations of 3 relaxed CFs. They all seem concentric with respect to the cluster centre, and spherical in appearance. They interpret these as evidence for sloshing, and find spiral characteristics in 2 of them. In the cold front sample of Ghizzardi et al. (2010), 10 of the relaxed morphology clusters also host cold fronts. We argue here that some CFs of this type could originate from shock mergers. In the SICF model, CFs are spherical, unlike the truncated CFs formed by ram pressure stripping or sloshing, so no special projection orientation is required. On the other hand, SICFs do not involve metallicity discontinuities, observed in some of these CFs. The observed contrasts of these three CFs in Owers et al. (2009) are quite uniform, with best fit values in the range 2.0 – 2.1 (with $\sim 20\%$ uncertainty) in all three, as expected for SICFs⁵.

The following characteristics are specific to SICFs, and could thus be used to differentiate between SICFs and CFs formed by other mechanisms. These are also predictions for SICFs that are expected to form at radii that are not observable today.

Morphology. SICFs are quasi-spherical around the source of the shocks. In contrast, for example, a galactic merger defines an orbit plane, and the corresponding perturbation (stripped material or sloshing and centre displacement) will create CFs parallel to this plane. In some sloshing scenarios (Ascasibar & Markevitch 2006) the CFs extend considerably above the plane, but would never cover

all viewing angles; an observed closed CF “ring” would strongly point towards an SICF. The statistical properties of a large CF sample could thus be used to distinguish between the different scenarios. Ghizzardi et al. (2010) identify 23 apparently relaxed clusters, 10 of which exhibit cold fronts. They find a *perfect* correlation between central entropy levels and cold fronts, with the 10 lowest central entropy clusters exhibiting cold fronts. This correlation is also consistent with convection of low entropy gas from the centre (Markevitch & Vikhlinin 2007; Keshet et al. 2009), but would require that all 10 CFs are viewed from a favorable viewing angle. We offer here an alternative interpretation, in which the low entropy and short cooling times imply relatively more active AGNs and consequently the formation of shocks on shorter periods (Ciotti et al. 2009). The SICFs naturally cover 4π of the sky, alleviating the viewing angle statistical requirement.

Amplitude. SICFs have distinct entropy and density contrasts that depend weakly on shock parameters; q is typically larger than ~ 1.4 (assuming $M_1 \geq 2$) and is always smaller than $q_{max} = 2.65$. This is consistent with observations.

Extent. If cluster oscillations, as described in § 5.2 are excited, SICF radii should be approximately logarithmically spaced. Any shock that expands and collides with the virial shock will create an SICF at the location of the virial shock, far beyond the core. The external SICFs are younger, and would appear sharper owing to less degradation due to the processes discussed in § 6.1. This concentric CF distribution thus resembles tree rings. Deep observations capable of detecting CFs at $r \sim 1$ Mpc are predicted to find SICFs (fig. 12). Such distant CFs occur naturally only in the SICF model (observations by Suzaku may be able to probe this range with sufficient quality in the near future; Hoshino et al. 2010).

Plasma diagnostics. Shocks are known to modify plasma properties in a non-linear manner, for example by accelerating particles to high energies and amplifying/generating magnetic fields. The plasmas on each side of an SICF may thus differ, being processed either by two shocks or by one, stronger shock. This may allow indirect detection of the CF, in particular if the two shocks were strong before the collision. For example, enhanced magnetic fields below the CF may be observable as excess synchrotron emission from radio relics that extend across the CF, in nearby clusters, using future high-resolution radio telescopes (MWA, LOFAR, SKA).

7 SUMMARY AND DISCUSSION

Our study consists of two parts. The first is a general, analytic discussion about cold fronts that form as a result of a merging between a primary and secondary shock propagating in the same direction. This is a novel mechanism to create cold fronts discussed here for the first time. The second part describes the possible relevance of this SICF mechanism in cluster environments using 1D spherical hydrodynamical simulations.

We have shown in § 2 that when shocks moving in the same direction merge they generate a CF. The density contrast across the CF is calculated as a function of the Mach

⁵ However, shocks sweeping over CFs could diminish their contrast towards $q \sim 2$, regardless of CF origin. A larger, more complete sample of CFs is needed to determine the origin/s of the relaxed population.

numbers of the two shocks. It is typically larger than 1.4 (if $M \gtrsim 2$), and is always smaller than $q_{max} = 2.65$. We support the analytical calculation by a detailed investigation of a shock tube planar hydrodynamical simulation.

In § 4 and § 5, using a 1D spherical hydrodynamic code, we demonstrate that SICFs in clusters are a natural consequence of shocks that are generated at centres of clusters. We entertain two ways to invoke shocks: by injecting large amounts of energy near the centre (corresponding to AGN outbursts), and by abruptly changing potential the well of the cluster (corresponding to merger events). Finally, by simulating cluster evolution from initial cosmological perturbations over a Hubble time we show that outgoing shocks that merge with the virial shock create very distinctive CFs. These shocks can be caused by a critical event (merger or explosion) but can also be invoked by stochastic oscillations of the cluster's core, caused by accretion of low angular momentum substructure that perturbs the core. We show that a reverberation mode exists in the haloes of galaxies and clusters that causes periodic merging between the virial shocks and secondary shocks, producing an SICF every cycle. The simulated SICF contrast is consistent with the theoretical predictions of § 2. A more thorough investigation of this potentially important mode, including its stability in 3D is left for future works.

We then discuss in § 6.1 the survivability and degradation in time of CFs after they are formed. The CF discontinuity is smeared over time by diffusion, at a rate that depends on the unknown nature and amplitude of magnetic fields. CFs are susceptible to heat-flux-driven buoyancy instability (Parrish & Quataert 2008, HBI;), which could align the magnetic field tangent to the CF and potentially moderate further diffusion. SICFs, like all other CFs, are subject to Richtmyer-Meshkov instabilities from subsequent shocks passing through the cluster. Such collisions also reduce the CF contrast until it reaches $q \sim 2$. Unlike most other CF models, an SICF is not expected to suffer from KHI.

The predicted properties of SICFs are presented in § 6.2, and reproduce some of the CF features discussed in Owers et al. (2009) and Ghizzardi et al. (2010). In particular, we suggest that CFs in relaxed clusters, with no evidence of mergers, shear, or chemical discontinuities, may have formed by shock collisions. We list the properties of SICFs that could distinguish them from CFs formed by other mechanisms. The SICF model predicts quasi-spherical CFs which are concentric about the cluster centre, with contrast $q \sim 2$, and possibly extending as far out as the virial shock. An observed closed (circular/oval) CF could only be an SICF. In the specific case of cluster reverberation, a distinct spacing pattern between CFs is expected. It may be possible to detect them indirectly, for example as discontinuities superimposed on peripheral radio emission.

Shocks originating from the cluster centre naturally occur in feedback models that are invoked to solve the overcooling problem. They are also formed by mergers of substructures with the BCG. Thus, SICFs should be a natural phenomenon in clusters. Further work is needed to assess how common SICFs are with respect to other types of CFs, and to characterize inner SICFs that could result, for example, from mergers between offset AGN shocks. The properties of SICFs in 3D will be pursued in future work.

ACKNOWLEDGEMENTS

We thank I. Parrish, Dušan Kereš and M. Markevitch for useful discussions and the referee, Trevor Ponman, for helpful suggestions. YB acknowledges the support of an ITC fellowship from the Harvard College Observatory. UK acknowledges support by NASA through Einstein Postdoctoral Fellowship grant number PF8-90059 awarded by the Chandra X-ray Centre, which is operated by the Smithsonian Astrophysical Observatory for NASA under contract NAS8-03060.

REFERENCES

- Ascasibar Y., Markevitch M., 2006, *ApJ*, 650, 102
- Bertschinger E., 1985, *ApJS*, 58, 39
- Binney J., Tremaine S., 1987, *Galactic dynamics*. Princeton, NJ, Princeton University Press, 1987, 747 p.
- Birnboim Y., Dekel A., 2003, *MNRAS*, 345, 349
- Birnboim Y., Dekel A., 2010, in preparation
- Birnboim Y., Dekel A., Neistein E., 2007, *MNRAS*, 380, 339
- Birzan L., Rafferty D. A., McNamara B. R., Wise M. W., Nulsen P. E. J., 2004, *ApJ*, 607, 800
- Bullock J. S., Dekel A., Kolatt T. S., Kravtsov A. V., Klypin A. A., Porciani C., Primack J. R., 2001, *ApJ*, 555, 240
- Bullock J. S., Kolatt T. S., Sigad Y., Somerville R. S., Kravtsov A. V., Klypin A. A., Primack J. R., Dekel A., 2001, *MNRAS*, 321, 559
- Burrows A., Livne E., Dessart L., Ott C. D., Murphy J., 2007, *ApJ*, 655, 416
- Cavagnolo K. W., Donahue M., Voit G. M., Sun M., 2009, *ApJS*, 182, 12
- Ciotti L., Ostriker J. P., 2007, *ApJ*, 665, 1038
- Ciotti L., Ostriker J. P., Proga D., 2009, *ApJ*, 699, 89
- David L. P., Slyz A., Jones C., Forman W., Vrtilek S. D., Arnaud K. A., 1993, *ApJ*, 412, 479
- Dekel A., Birnboim Y., Engel G., Freundlich J., Goerdt T., Mumcuoglu M., Neistein E., Pichon C., Teyssier R., Zinger E., 2009, *Nature*, 457, 451
- Edge A. C., Stewart G. C., Fabian A. C., Arnaud K. A., 1990, *MNRAS*, 245, 559
- Fabian A. C., Sanders J. S., Allen S. W., Crawford C. S., Iwasawa K., Johnstone R. M., Schmidt R. W., Taylor G. B., 2003, *MNRAS*, 344, L43
- Forman W., Jones C., Churazov E., Markevitch M., Nulsen P., Vikhlinin A., Begelman M., Böhringer H., Eilek J., Heinz S., Kraft R., Owen F., Pahre M., 2007, *ApJ*, 665, 1057
- Forman W., Nulsen P., Heinz S., Owen F., Eilek J., Vikhlinin A., Markevitch M., Kraft R., Churazov E., Jones C., 2005, *ApJ*, 635, 894
- George M. R., Fabian A. C., Sanders J. S., Young A. J., Russell H. R., 2009, *MNRAS*, 395, 657
- Ghizzardi S., Rossetti M., Molendi S., 2010, *ArXiv e-prints*
- Hernquist L., 1990, *ApJ*, 356, 359
- Hoshino A., Patrick Henry J., Sato K., Akamatsu H., Yokota W., Sasaki S., Ishisaki Y., Ohashi T., Bautz M., Fukazawa Y., Kawano N., Furuzawa A., Hayashida K., Tawa N., Hughes J. P., Kokubun M., Tamura T., 2010, *PASJ*, 62, 371

- Kereš D., Hernquist L., 2009, *ApJ*, 700, L1
- Keshet U., Markevitch M., Birnboim Y., Loeb A., 2009, ArXiv e-prints
- Kushnir D., Waxman E., Shvarts D., 2005, *ApJ*, 634, 407
- Landau L. D., Lifshitz E. M., 1959, *Fluid Mechanics*. Pergamon press, 1959
- Lazarian A., 2006, *ApJ*, 645, L25
- Leccardi A., Molendi S., 2008, *A&A*, 486, 359
- Markevitch M., 1998, *ApJ*, 504, 27
- Markevitch M., Ponman T. J., et al. 2000, *ApJ*, 541, 542
- Markevitch M., Vikhlinin A., 2007, *Phys. Rep.*, 443, 1
- Markevitch M., Vikhlinin A., Forman W. R., 2003, in S. Bowyer & C.-Y. Hwang ed., *Astronomical Society of the Pacific Conference Series Vol. 301 of Astronomical Society of the Pacific Conference Series, A High Resolution Picture of the Intracluster Gas*. pp 37–+
- Markevitch M., Vikhlinin A., Mazzotta P., 2001, *ApJ*, 562, L153
- McCarthy I. G., Bower R. G., Balogh M. L., Voit G. M., Pearce F. R., Theuns T., Babul A., Lacey C. G., Frenk C. S., 2007, *MNRAS*, 376, 497
- McNamara B. R., Nulsen P. E. J., 2007, *ARA&A*, 45, 117
- Navarro J. F., Frenk C. S., White S. D. M., 1997, *ApJ*, 490, 493
- Neistein E., van den Bosch F. C., Dekel A., 2006, *MNRAS*, 372, 933
- Owers M. S., Nulsen P. E. J., Couch W. J., Markevitch M., 2009, *ApJ*, 704, 1349
- Parrish I. J., Quataert E., 2008, *ApJ*, 677, L9
- Parrish I. J., Quataert E., Sharma P., 2009, *ApJ*, 703, 96
- Parrish I. J., Stone J. M., Lemaster N., 2008, *ApJ*, 688, 905
- Quataert E., 2008, *ApJ*, 673, 758
- Spiegel E. A., 1963, *ApJ*, 138, 216
- Sutherland R. S., Dopita M. A., 1993, *ApJS*, 88, 253
- Tucker W., Blanco P., Rappoport S., David L., Fabricant D., Falco E. E., Forman W., Dressler A., Ramella M., 1998, *ApJ*, 496, L5+
- Waxman E., Shvarts D., 1993, *Physics of Fluids A*, 5, 1035

APPENDIX A: SICF PARAMETERS

Using the thermal jump conditions, we find the density/temperature contrast across the CF given by

$$q \equiv \frac{\rho_{3i}}{\rho_{3o}} = \frac{M_0^2 M_1^2 (\gamma + 1) [M_f^2 (\gamma - 1) + 2]}{M_f^2 [M_0^2 (\gamma - 1) + 2] [M_1^2 (\gamma - 1) + 2]} \left\{ \frac{[(2M_0^2 - 1)\gamma + 1][(2M_1^2 - 1)\gamma + 1]}{(\gamma + 1)[(2M_f^2 - 1)\gamma + 1]} \right\}^{-1/\gamma},$$

where $M_f \sim M_0 M_1$ is the Mach number of the newly formed shock. It is determined by including the velocity jump conditions; for $\gamma = 5/3$ this yields

$$\left[4 \frac{5M_f^2 - 1}{(5M_0^2 - 1)(5M_1^2 - 1)} \right]^{1/5} = 1 + \frac{M_1^2 - 1}{\sqrt{(5M_1^2 - 1)(M_1^2 + 3)}} - \frac{4M_1(M_f - M_0)(M_0 M_f + 1)}{M_f \sqrt{(5M_0^2 - 1)(M_0^2 + 3)(5M_1^2 - 1)(M_1^2 + 3)}}, \quad (\text{A1})$$

which has three roots for M_f , only one of which is real.

In the strong primary shock regime $M_0 \gg 1$, appropriate for example for a secondary merging with a virial shock, q is the root of

$$q^{\frac{\gamma-1}{2}} + q^{\frac{\gamma}{2}} \sqrt{\frac{\gamma-1}{2\gamma}} = A + O(M_0^{-2}), \quad (\text{A2})$$

where

$$A \equiv \left(\frac{\gamma + 1}{\gamma - 1 + 2M_1^{-2}} \right)^{\frac{\gamma-1}{2}} + \left(\frac{\gamma + 1}{\gamma - 1 + 2M_1^{-2}} \right)^{\frac{\gamma}{2}} \frac{\left(M_1 - \frac{1}{M_1} \right) \frac{\gamma-1}{\sqrt{\gamma+1}} + \sqrt{\frac{\gamma^2-1}{2\gamma}}}{\sqrt{(2M_1^2 - 1)\gamma + 1}}.$$

The contrast reaches its maximal value q_{max} when M_1 satisfies $dA/dM_1 = 0$. This maximal value is a function of γ , as shown in Figure 3.

For $\gamma = 5/3$, Eqs. (A2) simplifies to

$$\left(\frac{M_1^2 + 3}{4M_1^2} q \right)^{1/3} \left(1 + \sqrt{\frac{q}{5}} \right) = 1 - \frac{1 - \frac{4M_1}{\sqrt{5}} - M_1^2}{\sqrt{(5M_1^2 - 1)(M_1^2 + 3)}}. \quad (\text{A3})$$

Maximizing the contrast yields $q_{max} = 2.653$, corresponding to $M_1 = 6.654$.

It is interesting to point out that the observed contrast q across an SICF could be used to impose an upper limit on γ , and hence constrain the equation of state. Figure 3 shows that q monotonically decreases with increasing γ in the relevant, $\gamma > 1.15$ regime. After an SICF is produced with some initial contrast $q \leq q_{max}$, its contrast typically declines in time as the CF is degraded by diffusion, convection, interactions with subsequent outgoing shocks, etc. Therefore, $q_{max}(\gamma) > q$ constrains γ . For example, an observed SICF contrast $q > 2.653$ ($q > 3.108$) would imply that $\gamma < 5/3$ ($\gamma < 4/3$), suggesting the abundance of cosmic rays where the shocks collided.